Tunable and giant valley-selective Hall effect in gapped bilayer graphene

Authors: Jianbo Yin[1,2,†,*], Cheng Tan[3,†], David Barcons-Ruiz[1], Iacopo Torre[1], Kenji Watanabe[4], Takashi Taniguchi[4], Justin C. W. Song[5], James Hone[3], Frank H. L. Koppens[1,6,*]

Affiliations:

[1]ICFO–Institut de Ciencies Fotoniques, The Barcelona Institute of Science and Technology, Castelldefels (Barcelona), Spain.

[2]Beijing Graphene Institute, Beijing, China

[3]Department of Mechanical Engineering, Columbia University, New York, New York 10027, USA.

[4]National Institute for Materials Science, Tsukuba, Japan

[5]Division of Physics and Applied Physics, Nanyang Technological University, 637371 Singapore, Singapore.

[6]ICREA–Institució Catalana de Recerça i Estudis Avancats, Barcelona, Spain.

[†]These authors contributed equally to this work

*Corresponding author. Email: jyin@icfo.net, frank.koppens@icfo.eu

Abstract:

Berry curvature is analogous to magnetic field but in momentum space and is commonly present in materials with non-trivial quantum geometry. It endows Bloch electrons with transverse anomalous velocities to produce Hall-like currents even in the absence of a magnetic field. We report the direct observation of *in situ* tunable valley-selective Hall effect (VSHE), where inversion symmetry, and thus the geometric phase of electrons, is controllable by an out-of-plane electric field. We use high-quality bilayer graphene with an intrinsic and tunable bandgap, illuminated by circularly polarized mid-infrared light and confirm that the observed Hall voltage arises from an optically-induced valley population. Compared with molybdenum disulfide (MoS$_2$), we find orders of magnitude larger VSHE, attributed to the inverse scaling of the Berry curvature with bandgap. By monitoring the valley-selective Hall conductivity, we study Berry curvature's evolution with bandgap. This *in situ* manipulation of VSHE paves the way for topological and quantum geometric opto-electronic devices, such as more robust switches and detectors.

One-Sentence Summary:
Bilayer graphene carries a giant photoinduced anomalous Hall conductance and can serve as quantum geometric infrared photodetector.

Main text:

In 1984, Berry proved that a quantum wave function acquires a geometric phase of $2N\pi$ (N as integer) after an adiabatic evolution along a loop in parameter space (*1*). This geometric phase was expressed as a surface integral of a vector field, coined as Berry curvature. Globally, the integral of Berry curvature over the full parameter space, representing the Chern number, defines the nature of specific topological states. Locally, Berry curvature $\Omega(\mathbf{k})$ behaves as an effective intrinsic field, analogous to magnetic field, but acting in momentum space. Berry curvature distorts the

conventional semiclassical trajectories of Bloch electrons in crystals to endow them with an anomalous velocity perpendicular to an applied electric field **E** (2–6):

$$\mathbf{v(k)} = \frac{\partial \epsilon(\mathbf{k})}{\hbar \partial \mathbf{k}} + \frac{q}{\hbar} \mathbf{E} \times \mathbf{\Omega(k)} \qquad (1)$$

where **v**, **k**, ϵ, **E**, q and $\hbar$ are electron velocity, wavevector, band energy, electric field, carrier charge and reduced Planck's constant, respectively.

Two-dimensional Dirac materials such as graphene and transition metal dichalcogenides (TMDs) are a particularly attractive platform for realizing a host of new topological and quantum geometrical responses (7). For instance, low-dissipation valley currents were inferred by measuring non-local signals in graphene-boron nitride (BN) superlattices and MoS_2 (8–11); under strong laser irradiation, graphene can exhibit a Floquet-driven anomalous Hall phase (12). No less notable, however, is gapped bilayer graphene (GBG), which can host enormous Berry curvature density at its band edges (Fig. 1B) which have been predicted to produce a giant anomalous (or valley-selective) Hall effect (13). Berry curvature in many materials is often thought to be fixed by its crystal configuration; by contrast, Berry curvature in bilayer graphene can be tailored externally by tuning the inter-layer potential, providing a versatile knob to study Berry curvature-driven quantum geometric phenomena. For example, in Refs. (14–17) non-local valley currents were reported in GBG, bilayer graphene-BN superlattice, and twisted double-bilayer graphene, respectively. However, nonlocal resistance fingerprints have also been predicted to originate from a spatially nonuniform gap profile (11, 18), and recent scanning gate imaging experiments found that non-local transport signals in graphene can also arise because of charge accumulation at the edges, and therefore may not necessarily have a bulk valley Hall effect origin (19). In contrast to the non-local measurements, direct Hall measurements by optical pumping can quantify the expected giant Hall conductivity in GBG, and trace the evolution of Berry curvature with gap and energy. Unlike in TMDs (20–22) direct observations of light-induced VSHE and its associated Berry curvature distribution have not been reported in gapped graphene-based systems.

Measurement design

In this work we directly probe the tunable VSHE in bilayer graphene with variable bandgap E_g from 0 to 0.125 eV, by valley polarizing carriers with circularly polarized infrared light. The concept is shown in Fig. 1A. First, we use top and bottom gates to apply displacement fields D_T and D_B, as further explained in the materials and methods (23, 24). The average of these two fields $\bar{D} = (D_B + D_T)/2$ adds energy bias between the two layer of bilayer graphene, which breaks inversion symmetry and controls E_g as well as the E_g-dependent Berry curvature, as shown in Fig. 1B (13). The displacement difference $\delta D = D_B - D_T$ controls the Fermi level E_F. Second, we selectively excite carriers in the K (or K′) valley with a right (or left) circularly polarized mid-infrared laser (25–29). This valley circular dichroism arises directly from the opposite orbital moments of electrons in valley K and K′ when inversion symmetry is broken enabling circularly polarized light to preferentially induce interband transitions in either K or K′ valleys, see also a golden rule calculation in Texts 1 & 7 of the supplementary materials (SM). When we subject the valley-polarized photocarriers to an electric field **E** from source-drain bias V_b, the anomalous velocity due to the Berry curvature $\mathbf{\Omega}$ induces a Hall voltage, as described by equation 1. We note that the valley imbalance is essential to observing a Hall voltage: Otherwise equal valley currents from the two valleys will cancel each other out, because they are driven by opposite $\mathbf{\Omega}$ (30). Third,

by independently tuning $\bar{D}$ and δD (Fig. S1), we can quantify the expected giant valley-selective Hall conductivity σ_H and study its dependence on E_g and E_F respectively. Therefore, our measurement can directly probe anomalous (geometric) currents in non-trivial quantum geometric materials with small bandgaps.

Spatial distributions of photoinduced valley-selective Hall voltage

A typical Hall device is shown in Fig. 1C and consists of ultraclean hexagonal BN (hBN)-encapsulated bilayer graphene, with monolayer (or few-layer) graphene as the semi-transparent top and bottom gates. The device design is optimized for probing the Hall voltage induced by optical illumination of the bulk of the device. The active area of the device is square-shaped, with graphite contacts placed at a relatively large distance to avoid spurious photovoltage generation at the contacts. The device is mounted in an optical cryostat (device temperature 33 K) with a focussed infrared light source (spot size of ~25μm), which can be scanned over the device surface while monitoring longitudinal (along $\mathbf{E}$ and noted by xx) and transverse (perpendicular to $\mathbf{E}$ and noted by yy) voltages. The photoinduced anomalous (or valley-selective) Hall voltage V_H is the transverse voltage difference between left and right circularly-polarized illuminations $V_H = V_{yy}(\circlearrowright)$ $- V_{yy}(\circlearrowleft)$, which is probed by a lock-in amplifier, while the polarization chirality is modulated by photoelastic modulator (PEM) at ~50 kHz (Fig. S2, and materials and methods). To confirm the origin of V_H, we also modulate the laser intensity (on/off) and measure the photocurrent $\Delta I_{xx} = I_{xx}(\text{on}) - I_{xx}(\text{off})$ at the longitudinal terminals, as well as the transverse photovoltage $\Delta V_C = V_C(\text{on}) - V_C(\text{off})$ between transverse terminals. The spatial distributions of V_H, ΔI_{xx} and ΔV_C are shown in Fig. 1, D to F. The monopolar spatial features of both V_H and ΔI_{xx} indicate that these signals arise from the bulk of the device; this contrasts with the bipolar spatial features of ΔV_C that we attribute to local built-in fields at graphene-electrode contacts.

Exciton states and bandgap-dependent VSHE

Data establishing the high quality and intrinsic bandgap of the device are presented in Fig. 2A, in which resistivity ρ_{xx} is recorded as a function of $\bar{D}$ and δD (see line traces in Fig. S4). Here, we use $\delta D \cdot \varepsilon_0 e^{-1}$ (ε_0 and e are vacuum permittivity and elementary charge, respectively) to quantify Fermi level sweeping as it equalizes to the gate-injected free-carrier density n_0 at $\bar{D}=0$. However, at $\bar{D} \neq 0$, the value of $\delta D \cdot \varepsilon_0 e^{-1}$ is larger than n_0 because the Fermi level needs to move across the band gap to induce free carriers. The $\bar{D}$-dependent high resistivity plateau when the Fermi level is inside the gap is shown in Fig. 2A and an instrument-limited value of 10^7 ohms at $\bar{D} > 0.8$ V nm^{-1} has been reached. This high resistivity rules out other conductive channels [e.g. hopping or a topological conductive channel (*31*)] and confirms the existence of an intrinsic gap. The relation between E_g and $\bar{D}$ is further extracted from temperature-dependent resistance measurements, as shown in Fig. 2B, Fig. S5 and SM Text 2. The Arrhenius plot in Fig. S5E shows thermally-activated band conduction for the full temperature range from 37 to 230 K, demonstrating that the device quality overcomes earlier-reported challenges in gapped Dirac materials that are related to impurity-mediated conduction (*14, 20*). The high quality is also echoed by the high E_g-dependent mobility μ that exceeds 100,000 cm^2 V^{-1} s^{-1} at $T < 30$ K (Fig. S6 and SM Text 3); a comprehensive device characterization that includes van der Pauw measurements can be found in SM Texts 2, 3 and 9.

The effect of infrared optical illumination is first studied by probing multiple exciton peaks, visible in the E_g-dependent photocurrent curves displayed in Fig. 2C. For increasing gap size, multiple exciton states resonate with incident photons, giving rise to enhanced interband absorption and photocurrent peaks (32). The exciton states as indicated by the left dashed line are further labelled by black crosses in Fig. 2B. The optical excitation of photocarriers manifests as a typical photoconductivity feature under source-drain bias V_b as indicated by the blue arrow in the I_{xx}-V_b curve (Fig. 2D). Photoconductivity is an essential precondition for the VSHE, which clearly differs from the photovoltaic, photo-thermoelectric and bolometric effects observed in monolayer and bilayer graphene (33).

In the photoconductive regime, central for the study in this work, the ΔI_{xx} and V_H are measured simultaneously as a function of E_g and E_F by tuning $\overline{D}$ and δD independently (Fig. 2, E and F and their linecuts in Fig. S7, photon energy $h\nu = 122.9$ meV and laser intensity $P = 1.4$ µW µm^{-2}). The dashed triangular zone indicates the region with the Fermi level inside the gap before applying V_b and illumination on the device, where ΔI_{xx} shows a relative uniform distribution until E_g approaches $h\nu$ and triggers resonant absorption at $E_g \sim 120$ meV, depicted by the blue arrow in Fig. 2E and Fig. S8. We note that the abrupt decline of ΔI_{xx} outside the triangular zone is mainly caused by a dramatic decrease of V_b (Fig. S9). In contrast to the observation of one resonant peak in ΔI_{xx}, V_H shows two peaks (indicated by two arrows in Fig. 2F). Besides one at $E_g \sim 120$ meV, an additional peak at $E_g \sim 10$ meV is formed by a rapid rise of V_H when E_g increases from zero, and a decline of V_H when E_g increases beyond 10 meV. Qualitatively, these features are expected from the inversion symmetry-breaking requirement of the VSHE, and the fast decline of Berry curvature with increasing E_g, as shown in Fig. 1B. A more quantitative analysis will follow later in the text. Another prominent feature is the presence of V_H outside the dashed triangular zone, such as the area around coordinate $(\delta D \cdot \varepsilon_0 e^{-1}, E_g) = (-1 \times 10^{11}$ cm^{-2}, 20 meV$)$ as indicated by a white arrow in Fig. 2F. This will be further discussed later in the text as well.

Fingerprints of VSHE

The VSHE has key fingerprints that arise from its dependence on in-plane electric field **E** and Berry curvature **Ω** (equation 1). The first is a linear V_H-V_b relation as shown in Fig. 3A when the laser is positioned in the middle of the device. Spatial scans are shown in Fig. S10 and reveal opposite signs of V_H for $V_b = \pm 40$ mV. The second fingerprint is the dependence of V_H on **Ω**, which is controlled by selectively exciting the K or K′ valley. Experimentally, we change the chirality modulation (bottom arrows in Fig. 3B and Fig. S2) to exchange the initially-excited valley, which causes a flip of V_H polarity (red circles in Fig. 3B and spatial scans in Fig. S3). In a control measurement with inversion symmetry preserved, that is, $\overline{D} = 0$, V_H only shows small and featureless signals (black circles in Fig. 3B, see materials and methods for more discussion), consistent with the fact that the absence of a bandgap erases the Berry curvature.

Next, we present a more quantitative analysis of the photoinduced valley-selective Hall conductivity σ_H, because we can vary several parameters in-situ such as photocarrier density n_{ph}, Fermi level E_F and the bandgap E_g. Here, $\sigma_H \approx \sigma_{xx} * V_H/V_{xx}$ [(20) and SM Text 4], with the following measured parameters under illumination: V_H, longitudinal conductivity σ_{xx}, and longitudinal voltage V_{xx}. With this, we can study the dependence of σ_H on n_{ph}, with n_{ph} obtained from the measured longitudinal photoconductivity $\Delta \sigma_{xx} = n_{ph} e \mu$ (see inset of Fig. 3C and SM Text 6). We find a non-linear increase of σ_H with n_{ph} (Fig. 3C). The initial fast rise agrees with theoretical predictions [(13) and SM Text 8] and shows a sensitive valley-selective Hall response

with n_{ph}. The data also show that σ_H can be tuned by several orders of magnitude by changing the light intensity within 1.4 μW μm^{-2}. Theoretical estimates (dashed lines) in Fig. 3C reveal that σ_H is very sensitive to the Fermi level E_F or gate-induced carrier density n_0. This will be discussed later in the text.

Evolution of σ_H

A full parameter dependence of σ_H can be obtained by tuning E_g (via $\bar{D}$) and the carrier density (via δD). As illustrated in Fig. 4A, the carrier density is proportional to $\Delta E = |E_F - E_{edge}|$, where E_{edge} represents band edges of conduction or valence bands (SM Text 5). In Fig. 4B, we focus on hole doping with $\Delta E = E_{edge} - E_F$ and plot the experimental σ_H versus E_g and ΔE. Our experimental data are consistent with simple theoretical estimates of intrinsic valley-selective Hall conductivity (*13*), as presented in Fig. 4C and SM Text 8. The agreement is notable given that no adjustable fitting parameters and only experiment-based n_{ph}, n_0 and E_g values are used in the theoretical estimate (Fig. S11).

Notably, the measured σ_H in Fig. 4B reaches large values of 0.04 e^2/h despite very weak illuminating power ($P = 1.4$ μW/μm^2, $h\nu = 122.9$ meV). This value is four orders of magnitude higher than that measured for MoS$_2$ at the same laser intensity (*20*). The large σ_H magnitudes arise from the giant values of Berry curvature that can be found in Dirac materials with very narrow gaps such as GBG (*13*). Indeed, when E_g is increased, we find that σ_H rapidly diminishes (see Fig. 4B and its line trace as red circles in Fig. 4D) by more than three orders of magnitude. This E_g-induced giant tunability of σ_H, consistent with that expected from intrinsic valley-selective Hall conductivity (*13*), highlights the extreme sensitivity of Berry curvature induced opto-electronics to gate-controlled E_g (see also Fig. 1B).

Another prominent feature we observed is a non-monotonic dependence of σ_H on ΔE as shown by the red circles in Fig. 4E (a horizontal line trace of Fig. 4B). Here we vary ΔE but use a small fixed value of E_g. We find that σ_H first increases by more than an order of magnitude, peaking at $\Delta E \approx 9$ meV, and then decreases. This dependence is consistent with theoretical estimates of σ_H based on the extracted experiment-based n_{ph} and n_0 as shown by blue crosses in Fig. 4E (line trace of Fig. 4C). A similar non-monotonic dependence can also be found in σ_H versus E_g (red circles in Fig. 4D), displaying a peak at $E_g \approx 10$ meV; this qualitative trend is also similarly mirrored by the intrinsic valley-selective Hall conductivity (blue crosses in Fig. 4D).

The agreement between experiment and intrinsic valley-selective Hall conductivity (*13*) can enable tracking of the quantum geometric properties of bilayer graphene. Even as the simple theoretical (intrinsic) estimates produce the same trends as the observed Hall conductivity, there exist some quantitative discrepancies; see, for example, Fig. 4, B to D. Indeed, other mechanisms such as skew scattering and side jumps may also be present (*4, 34*). Including these, in addition to other band structure effects, such as trigonal warping (*35*), may provide improved quantitative agreement with the observed σ_H .

Summary and prospects

The giant (0.04 e^2/h at $P = 1.4$ μW μm^{-2} and $h\nu = 122.9$ meV) and highly (gate) tunable σ_H response in our GBG devices contrasts sharply with that of the small σ_H found in other Dirac materials (e.g., MoS$_2$) (*20*). This makes GBG a promising platform for realizing a new "quantum geometric

photodetector" in the infrared and terahertz spectral range. Such a detector can use large longitudinal voltage bias to enhance the Hall photocurrent, but at the same time suffers nearly zero dark current at transverse Hall contacts, exhibiting a high signal-to-noise ratio.

References and Notes

1. M. V. Berry, Quantal phase factors accompanying adiabatic changes. *Proc. R. Soc. London. A. Math. Phys. Sci.* **392**, 45–57 (1984).

2. D. Xiao, M.-C. Chang, Q. Niu, Berry phase effects on electronic properties. *Rev. Mod. Phys.* **82**, 1959–2007 (2010).

3. R. Karplus, J. M. Luttinger, Hall effect in ferromagnetics. *Phys. Rev.* **95**, 1154–1160 (1954).

4. N. Nagaosa, J. Sinova, S. Onoda, A. H. MacDonald, N. P. Ong, Anomalous Hall effect. *Rev. Mod. Phys.* **82**, 1539–1592 (2010).

5. In addition to intrinsic processes, anomalous Hall effect may also be caused by extrinsic processes such as side jump and skew scattering.

6. M. C. Chang, Q. Niu, Berry phase, hyperorbits, and the Hofstadter spectrum. *Phys. Rev. Lett.* **75**, 1348–1351 (1995).

7. J. C. W. Song, P. Samutpraphoot, L. S. Levitov, Topological Bloch bands in graphene superlattices. *Proc. Natl. Acad. Sci. U. S. A.* **112**, 10879–10883 (2015).

8. R. V Gorbachev, J. C. W. Song, G. L. Yu, A. V Kretinin, F. Withers, Y. Cao, A. Mishchenko, I. V Grigorieva, K. S. Novoselov, L. S. Levitov, A. K. Geim, Detecting topological currents in graphene superlattices. *Science.* **346**, 448–451 (2014).

9. K. Komatsu, Y. Morita, E. Watanabe, D. Tsuya, K. Watanabe, T. Taniguchi, S. Moriyama, Observation of the quantum valley Hall state in ballistic graphene superlattices. *Sci. Adv.* **4**, eaaq0194 (2018).

10. Z. Wu, B. T. Zhou, X. Cai, P. Cheung, G.-B. Liu, M. Huang, J. Lin, T. Han, L. An, Y. Wang, S. Xu, G. Long, C. Cheng, K. T. Law, F. Zhang, N. Wang, Intrinsic valley Hall transport in atomically thin MoS_2. *Nat. Commun.* **10**, 611 (2019).

11. T. Aktor, J. H. Garcia, S. Roche, A.-P. Jauho, S. R. Power, Valley Hall effect and nonlocal resistance in locally gapped graphene. *Phys. Rev. B*. **103**, 115406 (2021).

12. J. W. McIver, B. Schulte, F.-U. Stein, T. Matsuyama, G. Jotzu, G. Meier, A. Cavalleri, Light-induced anomalous Hall effect in graphene. *Nat. Phys.* **16**, 38–41 (2020).

13. J. C. W. Song, M. A. Kats, Giant Hall Photoconductivity in Narrow-Gapped Dirac Materials. *Nano Lett.* **16**, 7346–7351 (2016).

14. Y. Shimazaki, M. Yamamoto, I. V. Borzenets, K. Watanabe, T. Taniguchi, S. Tarucha, Generation and detection of pure valley current by electrically induced Berry curvature in bilayer graphene. *Nat. Phys.* **11**, 1032–1036 (2015).

15. M. Sui, G. Chen, L. Ma, W. Y. Shan, D. Tian, K. Watanabe, T. Taniguchi, X. Jin, W. Yao, D. Xiao, Y. Zhang, Gate-tunable topological valley transport in bilayer graphene. *Nat. Phys.* **11**, 1027–1031 (2015).

16. K. Endo, K. Komatsu, T. Iwasaki, E. Watanabe, D. Tsuya, K. Watanabe, T. Taniguchi, Y. Noguchi, Y. Wakayama, Y. Morita, S. Moriyama, Topological valley currents in bilayer graphene/hexagonal boron nitride superlattices. *Appl. Phys. Lett.* **114**, 243105 (2019).

17. S. Sinha, P. C. Adak, R. S. S. Kanthi, B. L. Chittari, L. D. V. Sangani, K. Watanabe, T. Taniguchi, J. Jung, M. M. Deshmukh, Bulk valley transport and Berry curvature spreading at the edge of flat bands. *Nat. Commun.* **11**, 5548 (2020).

18. S. Roche, S. R. Power, B. K. Nikolic, J. H. Garcia, A.-P. Jauho, Have Mysterious Topological Valley Currents Been Observed in Graphene Superlattices? *J. Phys. Mater.* (2021), doi:10.1088/2515-7639/AC452A.

19. A. Aharon-Steinberg, A. Marguerite, D. J. Perello, K. Bagani, T. Holder, Y. Myasoedov, L. S. Levitov, A. K. Geim, E. Zeldov, Long-range nontopological edge currents in charge-neutral graphene. *Nature*, **593,** 528–534 (2021).

20. K. F. Mak, K. L. McGill, J. Park, P. L. McEuen, The valley Hall effect in MoS_2 transistors. *Science.* **344**, 1489–1492 (2014).

21. M. Onga, Y. Zhang, T. Ideue, Y. Iwasa, Exciton Hall effect in monolayer MoS_2. *Nat. Mater.* **16**, 1193–1197 (2017).

22. N. Ubrig, S. Jo, M. Philippi, D. Costanzo, H. Berger, A. B. Kuzmenko, A. F. Morpurgo, Microscopic Origin of the Valley Hall Effect in Transition Metal Dichalcogenides Revealed by Wavelength-Dependent Mapping. *Nano Lett.* **17**, 5719–5725 (2017).

23. Y. Zhang, T.-T. Tang, C. Girit, Z. Hao, M. C. Martin, A. Zettl, M. F. Crommie, Y. R. Shen, F. Wang, Direct observation of a widely tunable bandgap in bilayer graphene. *Nature.* **459**, 820–823 (2009).

24. J. B. Oostinga, H. B. Heersche, X. Liu, A. F. Morpurgo, L. M. K. Vandersypen, Gate-induced insulating state in bilayer graphene devices. *Nat. Mater.* **7**, 151–157 (2008).

25. W. Yao, D. Xiao, Q. Niu, Valley-dependent optoelectronics from inversion symmetry breaking. *Phys. Rev. B.* **77**, 235406 (2008).

26. H. Zeng, J. Dai, W. Yao, D. Xiao, X. Cui, Valley polarization in MoS_2 monolayers by optical pumping. *Nat. Nanotechnol.* **7**, 490–493 (2012).

27. K. F. Mak, K. He, J. Shan, T. F. Heinz, Control of valley polarization in monolayer MoS_2 by optical helicity. *Nat. Nanotechnol.* **7**, 494–498 (2012).

28. T. Cao, G. Wang, W. Han, H. Ye, C. Zhu, J. Shi, Q. Niu, P. Tan, E. Wang, B. Liu, J. Feng, Valley-selective circular dichroism of monolayer molybdenum disulphide. *Nat. Commun.* **3**, 887 (2012).

29. A. M. Jones, H. Yu, N. J. Ghimire, S. Wu, G. Aivazian, J. S. Ross, B. Zhao, J. Yan, D. G. Mandrus, D. Xiao, W. Yao, X. Xu, Optical generation of excitonic valley coherence in monolayer WSe_2. *Nat. Nanotechnol.* **8**, 634–638 (2013).

30. D. Xiao, W. Yao, Q. Niu, Valley-contrasting physics in graphene: Magnetic moment and topological transport. *Phys. Rev. Lett.* **99**, 236809 (2007).

31. L. Ju, Z. Shi, N. Nair, Y. Lv, C. Jin, J. Velasco, C. Ojeda-Aristizabal, H. A. Bechtel, M. C. Martin, A. Zettl, J. Analytis, F. Wang, Topological valley transport at bilayer graphene domain walls. *Nature.* **520**, 650–655 (2015).

32. L. Ju, L. Wang, T. Cao, T. Taniguchi, K. Watanabe, S. G. Louie, F. Rana, J. Park, J. Hone, F. Wang, P. L. McEuen, Tunable excitons in bilayer graphene. *Science*. **358**, 907–910 (2017).

33. N. M. Gabor, J. C. W. Song, Q. Ma, N. L. Nair, T. Taychatanapat, K. Watanabe, T. Taniguchi, L. S. Levitov, P. Jarillo-Herrero, Hot carrier-assisted intrinsic photoresponse in graphene. *Science*. **334**, 648–52 (2011).

34. T. Ando, Theory of Valley Hall Conductivity in Graphene with Gap. *J. Phys. Soc. Japan*. **84**, 114705 (2015).

35. S. Slizovskiy, E. McCann, M. Koshino, V. I. Fal'ko, Films of rhombohedral graphite as two-dimensional topological semimetals. *Commun. Phys.* **2**, 164 (2019).

36. S. Das Sarma, S. Adam, E. H. Hwang, E. Rossi, Electronic transport in two-dimensional graphene. *Rev. Mod. Phys.* **83**, 407–470 (2011).

37. K. J. Tielrooij, J. C. W. Song, S. A. Jensen, A. Centeno, A. Pesquera, A. Zurutuza Elorza, M. Bonn, L. S. Levitov, F. H. L. Koppens, Photoexcitation cascade and multiple hot-carrier generation in graphene. *Nat. Phys.* **9**, 248–252 (2013).

38. F. Zhang, A. H. MacDonald, E. J. Mele, Valley Chern numbers and boundary modes in gapped bilayer graphene. *Proc. Natl. Acad. Sci. U. S. A.* **110**, 10546–10551 (2013).

39. I. Torre, Diffusive solver: a diffusion-equations solver based on FEniCS. *arXiv:2011.04351* (2020).

Acknowledgments:

Supplementary Materials

Materials and Methods

Supplementary Text

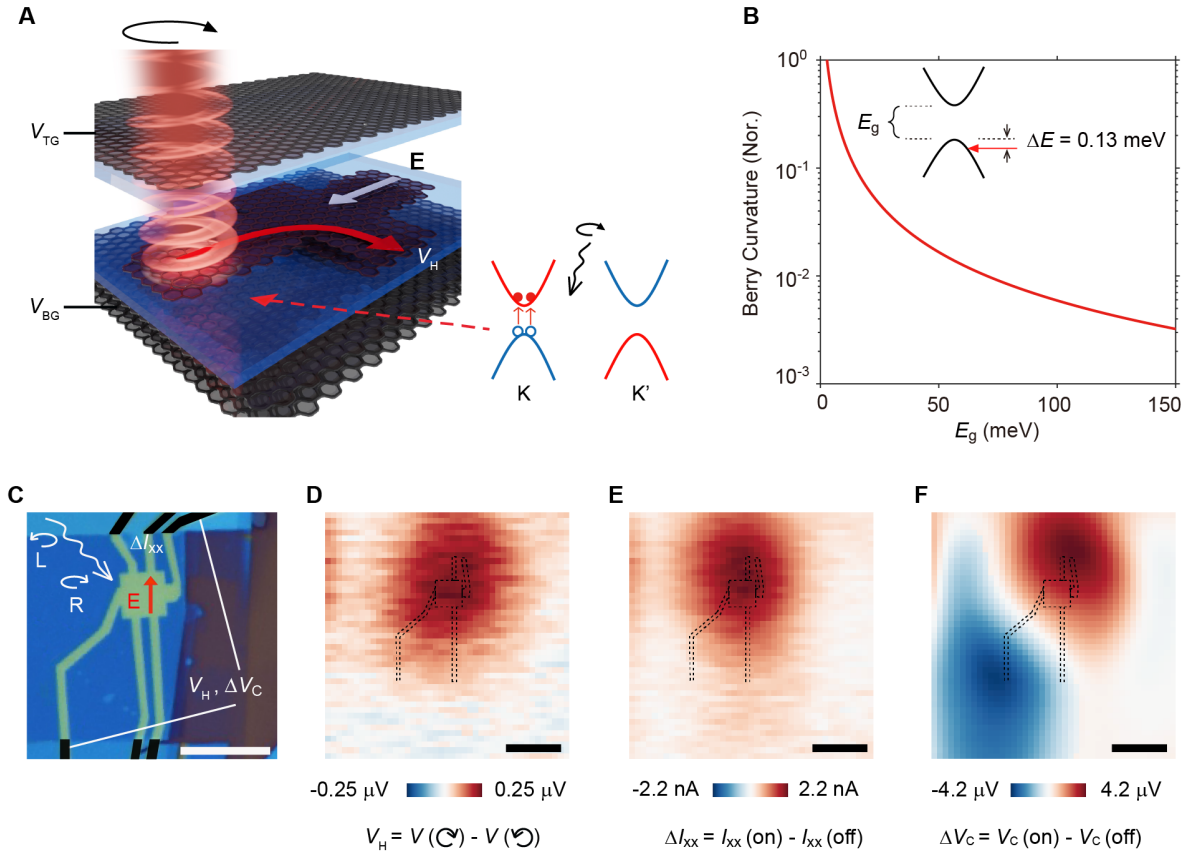Figs. S1 to S11

References (*36–39*)

Fig. 1. Valley-selective Hall effect in gapped bilayer graphene (GBG) driven by tunable Berry curvature. (**A**) Schematic illustration of valley-selective Hall measurement. Photocarriers at one valley are selectively excited by circularly polarized light. These photocarriers are driven by the in-plane electric field **E** and Berry curvature $\mathbf{\Omega}$, leading to a photoinduced anomalous Hall voltage. The blue and red colors of the illustrative band structure indicate polarities of the Berry curvature. (**B**) Fast evolution of $\mathbf{\Omega}$ with the gap size of GBG. The curve is based on equation S16 and describes $\mathbf{\Omega}$ values at bands with $\Delta E = 0.13$ meV away from band extremum. It is normalized by the value at $E_g = 3$ meV. Note that $\mathbf{\Omega}$ vanishes at zero gap. (**C**) Optical image of a bilayer graphene device. To reduce photovoltage at the bilayer graphene-electrode junction, all the electrodes are made of graphite, as indicated by the artificial black color. All of the device region shown in the figure overlaps with both top and bottom gates. L, left; R, right. (**D to F**) Spatial distributions of valley-selective Hall voltage (V_H), longitudinal photocurrent (ΔI_{xx}) and transverse photovoltage (ΔV_C), recorded by scanning device under a focused infrared laser with photon energy $h\nu = 123.7$ meV, intensity $P = 2.2$ μW μm^{-2}, and beam diameter of about 25 μm. V_H is collected as indicated by contacts at the furthest distance from the device bulk, while the chirality of the circularly-polarized light is modulated at 50 kHz. ΔI_{xx} and ΔV_C are collected with light intensity modulation at 177 Hz. Band gap $E_g = 35$ meV, source-drain bias $V_b = 50$ mV, gate-induced carrier density n_0=0. Dashed lines indicate device positions. Scale bars indicate 10 μm.
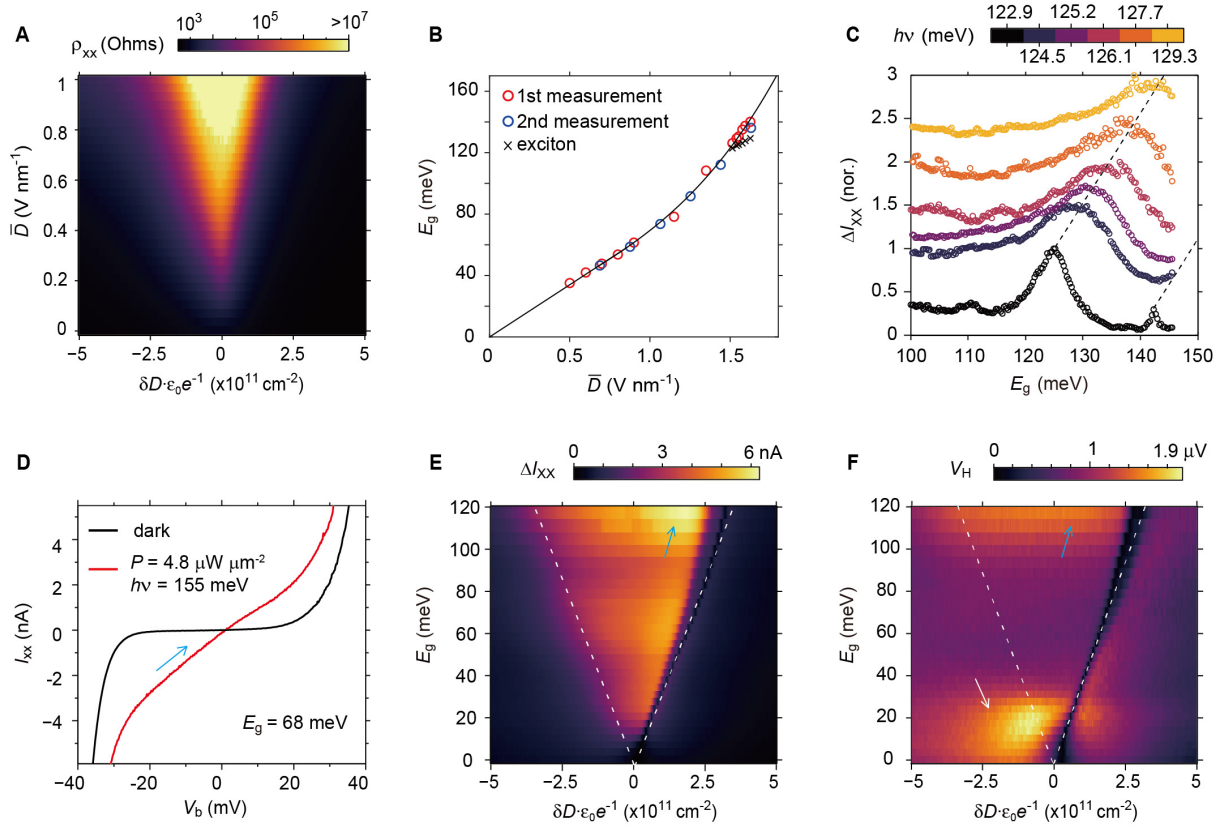
Fig. 2. Exciton states and gap-dependent valley-selective Hall voltage (V_H). (A) Two-dimensional map of the ρ_{xx} of GBG with respect to the average ($\overline{D}$) and difference (δD) of the top and bottom displacement fields. $\overline{D}$ and δD control band gap E_g and charge carrier density (and Fermi level E_F) respectively. At $\overline{D} = 0$, $\delta D \cdot \varepsilon_0 e^{-1}$ is equal to the gate-induced free carrier density (ε_0 and e are vacuum permittivity and elementary charge). $V_b = 1$ mV. **(B)** E_g of GBG at different $\overline{D}$. Red and blue circles indicate data from different measurements. Each point is extracted from a series of temperature-dependent transport measurements (Fig. S5). Black crosses indicate exciton peaks, as shown by the left dashed line in panel C. **(C)** Normalized photocurrents ΔI_{xx} of GBG excited by different infrared photons, with $V_b = 0$ and the Fermi level inside the gap. Photocurrent peaks arise from excitonic resonances, which are assigned to two excited states of excitons as indicated by the dashed lines. The energy values along the left line are labelled as black crosses in panel B. Incident laser intensity (P) increases linearly from 0.16 to 2.6 μW μm^{-2} with photon energy ($h\nu$) increasing from 122.9 to 129.3 meV, as indicated by the colour scale. The curves are shifted for clarity. **(D)** Current-bias (I_{xx}-V_b) curve of GBG in the dark and under illumination ($h\nu = 155.0$ meV, $P = 4.8$ μW μm^{-2}) with $E_g = 68$ meV and the Fermi level inside the gap before applying V_b and illumination. Slope increase (blue arrow) is a typical photoconductive feature. **(E and F)** ΔI_{xx} and V_H with respect to E_g and δD ($h\nu = 122.9$ meV, $P = 1.4$ μW μm^{-2}). The ΔI_{xx} and V_H are collected by modulating light intensity and chirality of circularly-polarized light, respectively. Two dashed lines indicate the insulating region that is due to the presence of a band gap. Blue arrows indicate ΔI_{xx} and V_H peaks that are due to absorption resonance. The white arrow shows and additional V_H peak and the presence of V_H outside the gap. The V_b introduces hole doping and

results in a resistance maximum around the right dashed line, along which ΔI_{xx} and hence V_H decreases (see SM Text 5). V_b increases from 1 to 89 mV with E_g (Fig. S9A).
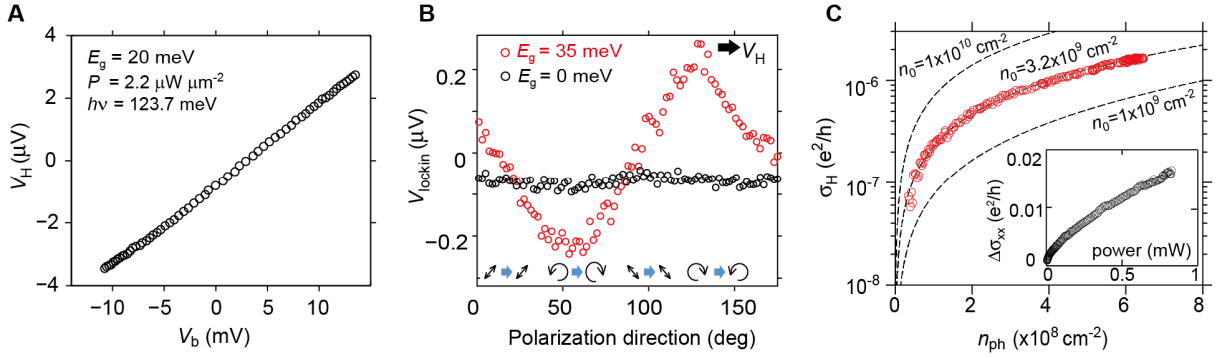

Fig. 3. Fingerprints of VSHE in GBG. (**A**) Linear dependence of V_H on V_b. The inset shows band gap E_g, laser intensity P and photon energy $h\nu$. The Fermi level is inside the gap before applying V_b and illumination on the device. (**B**) Lock-in amplifier signal V_{lockin} measured as a function of the polarization direction of light incident on PEM. Rotation of the polarization changes the chirality-modulation sequence from left-right to right-left (bottom arrows, see also Fig. S2). This exchanges the initially-excited valley (e.g. from K with $\mathbf{\Omega}$ to K′ with $-\mathbf{\Omega}$) and therefore flips V_H (indicated by the black arrow, see red circles with E_g at 35 meV). By contrast, linear-linear modulations at 5° and 95° do not generate valley imbalance and V_H. The same device without displacement field (thus without gap and measurable $\mathbf{\Omega}$) shows a featureless curve as presented by black circles. The shift here is due to a measurement circuit instead of the device response (see materials and methods). Laser parameters are $P \sim 0.26$ μW μm^{-2}, $h\nu = 123.7$ meV. (**C**) Fast growth of photoinduced valley-selective Hall conductivity σ_H with photocarrier density n_{ph}. Experimental results with $E_g = 122$ meV, $P = 1.4$ μW μm^{-2}, $h\nu = 122.9$ meV and $V_b = 70$ mV are shown by circles, which agree well with theoretical estimates of σ_H with fitting parameter (initial carrier density) $n_0 = 3.2 \times 10^9$ cm^{-2} as shown by the middle dashed line. Theoretical σ_H with $n_0 = 1 \times 10^9$ cm^{-2} and $n_0 = 1 \times 10^{10}$ cm^{-2} are also shown. These three dashed lines show strong correlation between σ_H and n_0. Photocarrier density n_{ph} is obtained by dividing $\Delta\sigma_{xx}$ (inset) by mobility and elementary charge. For dashed theoretical lines, we treated all photocarriers as being in a single valley consistent with absorption resonance (Fig. S11C)
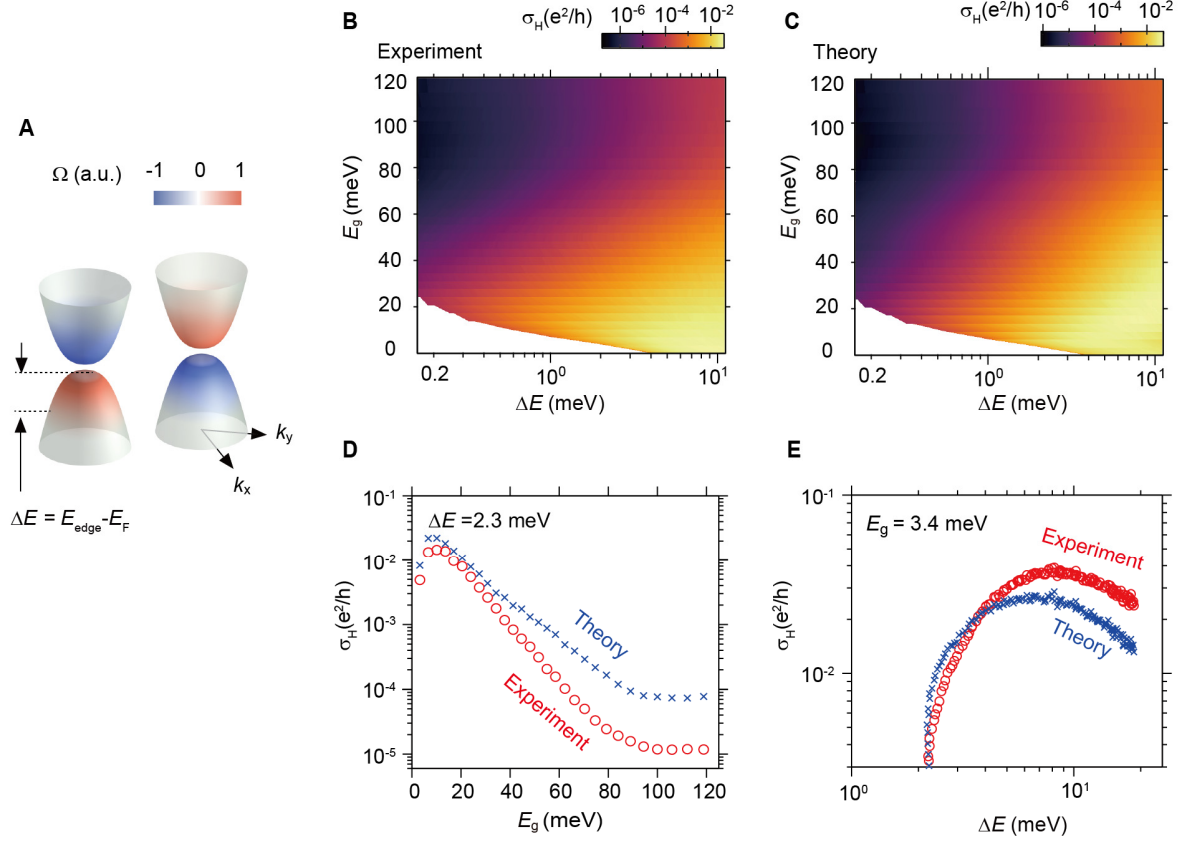
Fig. 4. Evolution of valley-selective Hall conductivity (σ_H). (**A**) Illustrative Berry curvature distribution in GBG. a.u., arbitrary units (**B**) Experimental dependence of σ_H with ΔE and E_g. The data at the lower-left corner are not accessible because of finite carrier density at low E_g induced by the bias doping effect. $h\nu$ =122.9 meV and $P = 1.4$ μW μm^{-2}. (**C**) Theoretical estimate of intrinsic photoinduced valley-selective Hall conductivity σ_H with E_g and ΔE. Here the photocarrier density n_{ph} was estimated using the measured longitudinal photoconductivity and device mobility; see also SM for discussion. (**D**) Vertical line traces of panel B as circles and panel C as crosses, showing abrupt decrease of σ_H with E_g. $\Delta E = 2.3$ meV. (**E**) Horizontal line traces of panel B and C, showing non-monotonic ΔE-dependent σ_H. $E_g = 3.4$ meV.

Supplementary Materials for

Tunable and giant valley selective Hall effect in gapped bilayer graphene

Jianbo Yin[†,*], Cheng Tan[†], David Barcons-Ruiz, Iacopo Torre, Kenji Watanabe, Takashi Taniguchi, Justin C. W. Song, James Hone, Frank H. L. Koppens[*]

*Corresponding author. Email: jyin@icfo.net, frank.koppens@icfo.eu

[†]These authors contributed equally to this work

This PDF file includes:

Materials and Methods
Supplementary Text 1 to 9
Figs. S1 to S12

Materials and Methods

Device fabrication

The Hall devices in our measurement consist of bilayer graphene, graphene (or thin graphite) as top gate, and graphite as bottom gates. All of these carbon layers are encapsulated and separated by boron nitride as shown in Fig. 1A and Fig. 1C. These atomically flat gates and dielectric materials guarantee a uniform gating and high breaking gate voltage. To fabricate the heterostructure in our devices, we sequentially picked up flakes of BN, graphene (or few-layer graphite) as top gate, BN, bilayer graphene as channel, graphene as electrode leads for device 1, BN, and graphite as backgate using a PPC/PDMS stamp. The PPC film with stacks were peeled off from PDMS stamp at around 110° C and left onto a Si/SiO2 substrate. The PPC was removed by vacuum annealing at $T = 350^{\circ}$ C. To shape the device and make one-dimensional contacts, CHF3/O2 plasma was used to etch away BN, graphene and graphite at a controllable speed with a hard mask by electron-beam lithography (EBL) of a hydrogen-silsesquioxane (HSQ) resist.

We have shown two typical devices in the paper. The spatial distributions in Fig. 1, Fig. S3 and Fig. S10 are measured from device 1 with graphene as top gate as shown in Fig. 1C. All the rest data and quantitative analysis are from device 2with very thin graphite (<10 nm) as top gate. The thicknesses of dielectric BN layers for top and bottom gates are 7.2 nm and 8.2 nm, respectively. To reduce phonon scattering, all our measurements were carried out at temperature $T = 33$ K, unless otherwise noted.

Displacement field and carrier density

By adjusting top and bottom gate voltages (V_{TG} and V_{BG}), we can tune the electric displacement fields $D_T = -\varepsilon_{t*}(V_{TG} - V^0_{TG})/d_t$ and $D_B = \varepsilon_b(V_{BG} - V^0_{BG})/d_b$, where ε_t, ε_b, d_t and d_b are top/bottom gate dielectric constant and top/bottom dielectric layer thickness, and V^0_{TG} (V^0_{BG}) are effective offset voltages of top (bottom) gates caused by initial environment-induced carrier doping (*23*). We note that V^0_{TG} (V^0_{BG}) are very limited in our high-quality devices due to the encapsulation as shown in Fig. S1a.

The average of these two fields, $\bar{D} = (D_B + D_T)/2$ breaks inversion symmetry and opens a band gap in bilayer graphene, while the difference of the two fields, $\delta D = D_B - D_T$ leads to carrier doping and thus Fermi level change. In bilayer graphene with $E_g = 0$, δD injects free charge carriers with density $n_0 = \delta D \cdot \varepsilon_0 e^{-1}$, where ε_0 and e are vacuum permittivity and elementary charge, respectively. However, for bilayer graphene with $E_g > 0$, density of free charge carrier $n_0 < \delta D \cdot \varepsilon_0 e^{-1}$ as some of the δD-injected charge carriers are immobile and drive Fermi level across the band gap. Therefore, by adjusting $\bar{D}$ and δD we could control band gap size and Fermi level independently. The relation between $\bar{D}$, δD V_{TG} and V_{BG} is shown in Fig. S1b.

Photoelastic modulator

To exclude a residual DC Hall voltage as shown in Fig. S2a, which is relatively large at neutralized states (usually due to impurities, device asymmetry, *et. al*) and drops strongly in conducting state (e.g. in the presence of relative large V_b or laser illumination), we use AC modulation of light polarization and a lock-in amplifier. In the measurement the chirality of circularly-polarized light is modulated by a photoelastic modulator (PEM), which transforms periodic electrical pulses (from pulse generator) into periodic forces (compression or stretching) on ZnSe crystal. Driven by these forces, the ZnSe crystal becomes birefringent periodically and is capable of retarding the light with

polarization direction parallel to the optical axis. By changing the electrical pulse intensity, one can adjust the retardation to $\lambda/4$ and turn linear polarization into circular polarization if the angle between polarization and optical axis is 45°, as shown in Fig. S2b and S2c. PEM is a resonant device with frequency $f \approx 50$ kHz. By locking the resonant frequency with the lockin-amplifier, one can probe the modulation-related signals (eg. valley selective Hall voltage V_H, when modulating the chirality of circular polarization) as shown by Fig. S2d. This measurement scheme is similar to that performed for the photocurrent ΔI_{xx} and conventional photovoltage ΔV_C measurements (Fig. S2e). The only difference is that chirality is modulated by PEM with intensity unchanged for V_H measurement, whereas intensity is modulated by chopper for ΔI_{xx} and ΔV_C measurement.

We note that the pulse generator of PEM works at resonant frequency and may contaminate the measurement circuit if not properly isolated. When this happens, sharing the same source with reference signal of lockin amplifier, the contamination can be picked up by the lockin amplifier and can give rise to a small constant background. This explains the offset of black circles in Fig. 3. We note that the measurements, used for quantitative analysis of valley selective Hall conductivity, are not contaminated after proper isolation.

Supplementary Text

Text 1. Valley selection rule

If carriers at K and K' valleys are balanced, their valley Hall voltages cancel out. Therefore, it is crucial to create carrier imbalance between two valleys in order to generate measurable valley selective Hall voltage. This means that time reversal symmetry needs to be broken (*25*). To realize this, we use a circularly-polarized infrared laser to selectively excite electrons at one valley. While this valley selective excitation has been extensively researched in transition metal dichalcogenides (TMD) (*26*). Our work demonstrates valley selective excitation in gapped bilayer graphene. This effect arises in analogy to the spin optical selection rule; instead of spin angular momentum, the valley circular dichroism arises directly from the opposite orbital moments of electrons in valley K and K' when inversion symmetry is broken enabling circularly polarized light to preferentially induce interband transitions in either K or K' valleys (*25*), see also detailed golden rule calculation in Text 7.

Text 2. Extraction of band gap.

The electrical bandgap E_g of our device is determined, for each displacement field, by fitting the available temperature-dependent resistance at the charge neutrality point $R(T)$ (Fig. S5a and S5b) to a thermal activation (TA) model:

$$R(T) = R_0 * \exp\left[\frac{E_g}{2k_B T}\right] \qquad (S1)$$

Where R_0 is a constant, k_B is Boltzmann constant. Our data shows good agreement with the TA model for $T > 100$ K (Fig. S5c and S5d) and therefore a reliable value of the E_g can be extracted at each $\bar{D}$. It is worthwhile to note that we used resistance data above 100 K to extract E_g, as at low temperature the resistance may be beyond the instrument range (see e.g., resistance data under high displacement field at 37 K in Fig. S5b). Arrhenius plots (natural logarithm of resistance as y

and T^{-1} as x) shows good linear shape as shown in Fig. S5e indicating that thermally activated conduction dominates the charge transport characteristics of our devices.

Text 3. Mobility μ

The carrier mobility μ of gapped bilayer graphene is calibrated by using two geometries: van der Pauw and two terminal geometries. In the van der Pauw geometry, we monitor the mobility while tuning temperature (T) as shown in Fig. S6a ($E_g = 0$ meV and $n_0 = 1.5 \times 10^{12}$ cm^{-2}), S6b ($E_g = 0$ meV and $n_0 = -1.5 \times 10^{12}$ cm^{-2}) and S6c ($E_g \approx 40$ meV and $n_0 = -4 \times 10^{12}$ cm^{-2}). At temperature lower than 24~27 K as indicated by dashed lines, the gapped bilayer graphene device displays very small voltage drops across the device, indicative of a transition to a possible ballistic regime; this is consistent with the high quality of our devices. Indeed, even at higher temperatures, e.g., at 33 K, our device already shows high electron mobility of 128,500 cm^2 V^{-1} s^{-1} for $E_g=0$ meV (Fig. S6a), high hole mobility of 54,260 cm^2 V^{-1} s^{-1} for $E_g=0$ meV (Fig. S6b) and hole mobility of 37,660 cm^2 V^{-1} s^{-1} for $E_g \approx 40$ meV (Fig. S6c). The decreasing trend of μ with E_g will be further discussed below.

The two-terminal transport data are measured at $T = 33$ K. The mobilities are fitted based on equation:

$$\rho = \frac{1}{n_0 \mu e} + \rho_c \qquad (S2)$$

where ρ, ρ_c, n_0 and e are resistivity, constant contact resistivity, carrier density and elementary charge, respectively. The resultant electron mobility μ_e and hole mobility μ_h are shown in Fig. S6d in logarithmic scale and Fig. S6e in linear scale. In these two figures, red (μ_e) and black (μ_h) circles (E_g range of 0 ~ 70 meV) correspond to measurement with source-drain bias $V_b = 1$ mV as shown in Fig. 2A, while orange (μ_e) and blue (μ_h) circles (E_g range of 0 ~ 120 meV) correspond to data from the similar measurement as shown in Fig. 2E with larger V_b (see Fig. S9a). Although with different V_b, these two sets of data show very similar mobility results, especially at the hole side. We note that the mobility magnitudes obtained in Fig S6d and S6e (two terminals) are consistent with those in Fig. S6a, S6b and S6c (van der Pauw measurement). More importantly, the decreasing trend of mobility with gap size provides insights into transport of gapped bilayer graphene: electron mobility drops by one order of magnitude as gap increases from 0 to 120 meV, while hole mobility drops even faster by two orders of magnitude.

Text 4. Experimental valley selective Hall conductivity

Hall conductivity σ_H in 2D system follows the equation:

$$\begin{pmatrix} j_{xx} \\ j_{yy} \end{pmatrix} = \begin{pmatrix} \sigma_{xx} & \sigma_{xy} \\ \sigma_{yx} & \sigma_{yy} \end{pmatrix} \begin{pmatrix} E_{xx} \\ E_{yy} \end{pmatrix} \qquad (S3)$$

where j and E are current density and electrical field, subscript xx and yy denote longitudinal and transverse directions. We have $\sigma_H = \sigma_{xy} = -\sigma_{yx}$, $\sigma_{xx} = \sigma_{yy}$, $j = I/W$, and $E = V/L$ with I, W, V and L as current, width, voltage and length respectively. With these relations, equation S3 gives:

$$\begin{pmatrix} I_{xx}/W_{xx} \\ I_{yy}/W_{yy} \end{pmatrix} = \begin{pmatrix} \sigma_{xx} & \sigma_H \\ -\sigma_H & \sigma_{xx} \end{pmatrix} \begin{pmatrix} V_{xx}/L_{xx} \\ V_{yy}/L_{yy} \end{pmatrix} \qquad (S4)$$

$$\frac{I_{yy}}{W_{yy}} = -\frac{\sigma_H V_{xx}}{L_{xx}} + \frac{\sigma_{xx} V_{yy}}{L_{yy}} \qquad (S5)$$

Given that (effective) length between source and drain is similar with that between two Hall bars $L_{xx} \sim L_{yy}$, and $V_{yy} = V_H$ in Hall measurement, we write:

$$I_{yy} * L_{yy}/W_{yy} = -\sigma_H V_{xx} + \sigma_{xx} V_H \qquad (S6)$$

Due to the high impedance of voltmeter (R_{imp}) and small voltage at Hall bars, I_{yy} is usually negligible (For example, it is 1 to 4 orders of magnitude smaller than $\sigma_{xx}V_H$ for different $\bar{D}$ and δD parameters in our measurement), which gives (see also Ref. 19):

$$\sigma_H \approx \sigma_{xx} * V_H/V_{xx} \qquad (S7)$$

The source-drain voltage V_{xx} and longitudinal conductivity $\sigma_{xx, light}$ with infrared light on are shown in Fig. S9a and Fig. S9b. These two data are measured at the same time with V_H in Fig. 2F, which guarantees a precise calibration of valley selective Hall conductivity σ_H. By using equation S7, we can calculate σ_H distribution with E_g and δD. In order to understand the evolution of σ_H, we have shown its distribution with E_g and energy difference to band edge $\Delta E = \left| E_{edge} - E_F \right|$ as shown in Fig. 4A and 4B. The ΔE is linked to δD via n_0 (n_0 as initial carrier density before photoexcitation, Fig. S11) as explained below.

Text 5. Link between δD, n_0 and ΔE

In the V_H measurement, the source-drain bias V_b values (Fig. S9a) used are larger than that used in ρ_{xx} calibration (Fig. 2A), especially when V_b is inside the dashed triangle zone of Fig. S9a. This positive source-drain bias V_b equivalently introduces charge carriers (e.g. holes here) into the sample. This doping can be compensated by increasing ΔD (injecting electrons). As result of the compensation, maximum resistance appears at the right border of the triangle area, around the right dashed line in Fig. 2F. When approaching this region, the resistance increases fast, leading to fast decline of ΔI_{xx} and hence fast drop of V_H (see Fig. 2E & 2F). The details of the bias-induced doping are as follows.

For a neutralized gapped state, the top gate voltage V_{TG} (eg. $V_{TG} > 0$) is balanced by a negative bottom gate voltage. Applying a positive source-drain bias ($V_b > 0$) weakens the gating effect of top gate (suppose $V_{TG} > 0$) by decreasing the equivalent gate voltage to $V_{TG} - V_b$. Meanwhile, it strengthens the back gate (now is negative) by increasing the amplitude of equivalent gate voltage. More negative back gate voltage and less positive top gate voltage both mean that more holes are injected to gapped bilayer graphene. This doping is inevitable if source-drain bias is applied.

The doped charge carriers elevate $\sigma_{xx,dark}$ (longitudinal conductivity before photoexcitation), which shows 10^{-7} to 10^{-5} S in the triangle zone as indicated by dashed lines in Fig. S9c. To quantify the total carrier density (n_0), we use equation $\sigma_{xx} = n_0 e \mu_h$ to calculate data in the hole-doped state as shown in trapezoid zone in Fig. S11a. Here, we are interested in hole doped region, and have used μ_h as shown by the blue circles in Fig. S6d, with assumption that μ_h is independent of hole carrier density for each band gap.

The resultant n_0 values in Fig. S11 are further used for calculating the corresponding Fermi level E_F. In bilayer graphene without a gap, E_F follows equation (36):

$$E_F = \text{sign}(n_0) * 2\pi\hbar^2 n_0 / (m_{\text{eff}} g_s g_v) \qquad (S8)$$

where effective mess $m_{\text{eff}} = 0.03 m_e$ with m_e as electron mass, $\hbar$ is reduced Plank constant, and g_s = 2 and g_v = 2 are spin and valley degeneracy. With the presence of a gap, we can estimate the energy difference ΔE between Fermi level E_F and band edge E_{edge}:

$$\Delta E = |E_{\text{edge}} - E_F| \approx 2\pi\hbar^2 * |n_0| / (m_{\text{eff}} g_s g_v) \qquad (S9)$$

Note that we have ignored the change of band profile when E_g increases, so ΔE is more precise at small gap.

With the link between δD, n_0 and ΔE, we have focused on the hole-doped side as shown by the trapezoid in Fig. S11, and presented the corresponding experimental dependence of σ_H on ΔE and E_g in Fig. 4B.

Text 6. Photocarrier density (n_{ph}) calculation

The total photocarrier density (n_{ph}) including photocarriers at both valleys satisfies equation $\Delta\sigma_{xx} = n_{\text{ph}} e \mu_{\text{ave}}$, in which $\Delta\sigma_{xx}$ is the increase of longitudinal conductivity due to illumination as shown in Fig. S9d ($\Delta\sigma_{xx} = \sigma_{xx,\text{light}} - \sigma_{xx,\text{dark}}$ with $\sigma_{xx,\text{light}}$ and $\sigma_{xx,\text{dark}}$ as shown in Fig. S9b and S9c), and the mobility μ_{ave} here is an average mobility of electron and hole: $\mu_{\text{ave}} = (\mu_e + \mu_h)/2$ (with μ_e and μ_h as shown by orange and blue circles in Fig. S6d) as photocarriers include both electrons and holes. By assuming that μ_{ave} only varies with E_g and is independent of n_0, we have calculated n_{ph} by dividing $\Delta\sigma_{xx}$ by μ_{ave} at each value of energy gap, as shown in Fig. S11b. Note that we have focused on hole-doped region here as shown by the trapezoid zone in Fig. S11b. The n_{ph} here includes initial photo-excited carriers and secondary hot carriers that arise from electron-electron scattering during the thermalization (37). The total photoexcited carrier density is highly E_g - and n_0- dependent, which explains the non-uniform distribution of n_{ph} in Fig. S11b.

Text 7. Valley imbalance of photocarriers

For bilayer graphene, absorption of circularly-polarized light causes valley imbalance of photocarriers $\delta n = n_{\text{ph}}^K - n_{\text{ph}}^{K'}$, where n_{ph}^K ($n_{\text{ph}}^{K'}$) is photocarrier density at K (K') valley and $n_{\text{ph}}^K + n_{\text{ph}}^{K'} = n_{\text{ph}}$. For simplicity and clarity, in what follows we use a simple two-band model for gapped bilayer graphene $H = \boldsymbol{d}(\boldsymbol{p}) \cdot \boldsymbol{\sigma}$, with (38)

$$\boldsymbol{d}(\boldsymbol{p}) = \left(\frac{v^2}{\gamma_1}[p_y^2 - p_x^2], \frac{2v^2}{\gamma_1} p_y p_x \zeta, \Delta \right) \qquad (S10)$$

Here $\boldsymbol{\sigma} = (\sigma_x, \sigma_y, \sigma_z)$ are the Pauli matrices, $\zeta = \pm 1$ for valley K and K', v is the velocity in monolayer graphene, and γ_1 is the interlayer coupling. We now turn to calculate the imbalance ratio $\delta n / n_{\text{ph}}$. Using Fermi's golden rule [see e.g., Ref (13)], we find the rate of electron-hole pair generation rate in each valley and each spin for circularly polarized incident light is

$$W_\zeta = \frac{e^2 |E_{\text{light}}|^2}{8\hbar^2\omega} \left(\frac{2\Delta}{\hbar\omega} + \zeta d \right)^2 \qquad (S11)$$

Where $d = \pm 1$ for left and right circularly polarized light, E_{light} represents electrical field intensity of light, $\Delta = E_g/2$ is half band gap, ω is angular frequency of light, and $\hbar\omega \geq 2\Delta$.

With illumination of left (or right) circularly polarized light, the generation of electron-hole pairs in K and K' valleys are asymmetric, which gives the generation rate of valley imbalance (per spin) as

$$\frac{d\delta n}{dt} = 2(W_K - W_{K'}) = 2d \frac{e^2 |E_{\text{light}}|^2}{\hbar^2 \omega} \frac{\Delta}{\hbar\omega} \qquad (S12)$$

Where the factor 2 here accounts for the generation of electrons and holes in the photoexcitation process. Similarly, the generation rate for total excited photocarrier density (per spin) follows as:

$$\frac{dn_{ph}}{dt} = 2(W_K + W_{K'}) = \frac{e^2 |E_{\text{light}}|^2}{2\hbar^2 \omega} \left[\left(\frac{2\Delta}{\hbar\omega}\right)^2 + 1 \right] \qquad (S13)$$

where we have noted $d^2 = 1$. The ratio of imbalance rate to total photocarriers rate at both valleys is:

$$\frac{\frac{d\delta n}{dt}}{\frac{dn_{ph}}{dt}} = \frac{4d\left(\frac{\Delta}{\hbar\omega}\right)}{\left[\left(\frac{2\Delta}{\hbar\omega}\right)^2 + 1 \right]} \qquad (S14)$$

As an illustration of the effect of photon frequency and gap size on the valley imbalance, we can use Eq. (S14) to obtain a simple estimate of the valley imbalance population (for a given total photoexcited carrier density). Assuming that the relaxation of the photo-excited carriers is dominated by intra-valley processes, and writing $\Delta = E_g/2$, we estimate:

$$\frac{\delta n}{n_{ph}} = \frac{2d\left(\frac{E_g}{\hbar\omega}\right)}{\left(\frac{E_g}{\hbar\omega}\right)^2 + 1} \qquad (S15)$$

For constant photon energy, such as $\hbar\omega = 122.9$ meV in our experiment, the ratio in S15 grows linearly with E_g when $(E_g/\hbar\omega)^2 \ll 1$. When E_g becomes larger and approaches $\hbar\omega$, $\delta n/n_{\text{ph}}$ rises sub-linearly and saturates to 1, as shown in Fig. S11c.

Text 8. Intrinsic photoinduced valley selective Hall conductivity

For the convenience of the reader, here we discuss the photoinduced Hall conductivity σ_H for gapped bilayer graphene arising from the anomalous velocity. The Berry curvature distributions at K and K' valley of gapped bilayer graphene follows (38):

$$\Omega_{\pm}^{\zeta}(\mathbf{p}) = \pm \zeta \frac{2\hbar^2 \Delta \gamma_1 v^4 |\mathbf{p}|^2}{(v^4 |\mathbf{p}|^4 + \gamma_1^2 \Delta^2)^{3/2}} \qquad (S16)$$

where $\pm$ denotes the conduction and valence bands, $\zeta = \pm 1$ denotes K and K' valleys, $\Delta = E_g/2$ is half of the band gap, v is the velocity in monolayer graphene, $\gamma_1 = 0.38$ eV is the interlayer coupling, $\mathbf{p}$ is momentum. From equation 1 in the main text and equation $j = \sigma * E$, valley selective Hall conductivity σ_H from the Berry curvature distribution can be written as:

$$\sigma_{\mathrm{H}} = \frac{Ne^2}{h}\left[\sum_{\mathbf{p},\pm} f_{\pm}^{\mathrm{K}}(\mathbf{p})\Omega_{\pm}^{\mathrm{K}}(\mathbf{p}) + \sum_{\mathbf{p},\pm} f_{\pm}^{\mathrm{K}'}(\mathbf{p})\Omega_{\pm}^{\mathrm{K}'}(\mathbf{p})\right] \qquad (S17)$$

where N = 2 denotes spin degeneracy, f is distribution function of carriers. Under photoexcitation, f describes the quasi-Fermi level distribution in the conduction and valence band (at K valley as example):

$$f_{\pm}^{\mathrm{K}}(\mathbf{p}) = [1 + e^{\beta(\varepsilon_{\mathbf{p}}^{\pm} - \mu_{\pm,\mathrm{K}})}]^{-1} \qquad (S18)$$

Where $\pm$ denotes the function for conduction and valence bands, $\beta = 1/k_{\mathrm{B}}T$ with k_{B} and T as Boltzmann constant and temperature, $\mu_{\pm,\mathrm{K}}$ is electron/hole quasi-Fermi levels at K valley, and $\varepsilon^{\pm}$ is conduction/valence band dispersion. The total photoexcited carrier density is n_{ph} and the initial carrier density before excitation is n_0 as described above.

For gapped bilayer graphene with small band gap, $\varepsilon^{\pm}$ can be written as:

$$\varepsilon^{\pm} = \pm\sqrt{v^4|\mathbf{p}|^4/\gamma_1^2 + \Delta^2} \qquad (S19)$$

Using equation S17, the carrier distributions multiplied by Berry curvatures yield:

$$\sigma_{\mathrm{H}} = \frac{Ne^2}{h}\left[G_{\mathrm{K}}\left(\frac{n_{\mathrm{ph,spin}}^{\mathrm{K}}}{2}\right) + G_{\mathrm{K}'}\left(\frac{n_{\mathrm{ph,spin}}^{\mathrm{K}'}}{2}\right)\right] \qquad (S20)$$

$$G_{\zeta}(x) = \zeta\left\{1 - \left[\frac{(\tilde{n}n_1)^{1/2}}{\sqrt{x^2 + \tilde{n}n_1}} + \frac{(\tilde{n}n_1)^{1/2}}{\sqrt{(x + n_{0,\mathrm{sp,val}})^2 + \tilde{n}n_1}}\right]\right\} \qquad (S21)$$

where $n_{\mathrm{ph,spin}}^{\mathrm{K}}$ ($n_{\mathrm{ph,spin}}^{\mathrm{K}'}$) are photocarrier density at K (K') valley per spin, $n_{0,\mathrm{sp,val}}$ is initial carrier density per valley and per spin, G_{ζ} with $\zeta = \pm 1$ denote contributions of the K and K' valleys respectively, and $\tilde{n} = \Delta^2/(16\pi v^2\hbar^2)$ depends on gap size $E_{\mathrm{g}} = 2\Delta$, v, and $\hbar$, $n_1 = \gamma_1^2/(4\pi v^2\hbar^2)$. This analysis is consistent with Ref. (13).

As seen from equations above, σ_{H} depends on four variables, including Δ (or $E_{\mathrm{g}}/2$), $n_{\mathrm{ph,spin}}^{\mathrm{K}}$, $n_{\mathrm{ph,spin}}^{\mathrm{K}'}$ and $n_{0,\mathrm{sp,val}}$. At each experimental point with coordinate ($\delta D \cdot \varepsilon_0 e^{-1}$, E_{g}) as shown in Fig. S9, these four variables can be extracted to calculate the theoretical estimate in Fig. 4C via equations S20 and S21. In particular, at each coordinate ($\delta D \cdot \varepsilon_0 e^{-1}$, E_{g}), n_0 and n_{ph} values were extracted as shown in Fig. S11a and S11b as explained before. n_0 is valley- and spin-independent and therefore is distributed equally into valleys and spins ($n_{0,\mathrm{sp,val}} = n_0/4$). n_{ph} is spin-independent but valley-dependent. It is distributed into two valleys based on relation in Fig. S11c, and then distributed equally into two spins ($n_{\mathrm{ph}} = n_{\mathrm{ph}}^{\mathrm{K}} + n_{\mathrm{ph}}^{\mathrm{K}'}$, where $n_{\mathrm{ph}}^{\mathrm{K}} = 2 * n_{\mathrm{ph,spin}}^{\mathrm{K}}$ and $n_{\mathrm{ph}}^{\mathrm{K}'} = 2 * n_{\mathrm{ph,spin}}^{\mathrm{K}'}$). With all these values (E_{g}, $n_{\mathrm{ph,spin}}^{\mathrm{K}}$, $n_{\mathrm{ph,spin}}^{\mathrm{K}'}$ and $n_{0,\mathrm{sp,val}}$) from experiment, the theoretical σ_{H} values are calculated based on equations S20 and S21. By linking $\delta D \cdot \varepsilon_0 e^{-1}$ - E_{g} axes

to ΔE - E_g axis in the same fashion as shown in Fig. 4B, we display theoretical estimates for the (intrinsic) valley selective Hall conductivity σ_H values in Fig. 4C.

We note that Fig. 4B and 4C are supported by the same underlying n_{ph} matrix (Fig. S11b), that varies at different coordinates. It is remarkable that the theoretical plot of Fig. 4C closely mirrors that found in the experiment in Fig. 4B. This close concordance between the two provides evidence that Berry curvature is essential for the σ_H values for our devices. We further note that when E_g approaches photon energy, the magnitude of n_{ph} increases likely due to absorption resonance (Fig. S8). This explains the rather flat trend in σ_H when $E_g > 100$ meV as shown in Fig. 4D: The increase of n_{ph} elevates the magnitude of σ_H (Fig. 3C), competes with the E_g - dependent declining trend in σ_H and hence results in flatness.

Text 9. Van der Pauw (vdPw) resistance R_{34} vs. longitudinal resistivity ρ_{xx}

As shown in Fig. S12, the vdPw resistance R_{34}, which is obtained by dividing the measured voltage at terminal 3 and 4 by the current injected from 1 to 2, is non-zero. Although it is challenging to differentiate ohmic contribution from non-ohmic due to small l/w ratio, it is useful to examine the scaling of R_{34} with ρ_{xx}. We find a parameter regime that scales as $R_{34} \propto \rho^3_{xx}$. Note that conventional ohmic contributions are expected to scale linearly with ρ_{xx}. This cubic scaling at low ρ_{xx} suggests that there is at least one regime that displays a non-ohmic contribution to R_{34}. We note that these results are only indicative, given the very small and non-ideal l/w ratio (about 0.5) of our device (which was designed for photoinduced VSHE and not for nonlocal measurements).

It is instructive to compare the conditions under which photo-induced anomalous Hall currents (from the VSHE) manifest with that of the non-ohmic contributions to vdPw measurements (as shown in Fig. S12). As we now explain, photo-induced anomalous Hall currents occur under different experimental conditions as compared with the vdPw measurements (and by extension, photo-induced anomalous Hall currents are also distinct from that of nonlocal resistance measurements in long Hall bars in GBG (*14, 15*). Importantly, photo-induced anomalous Hall currents arise when GBG is pushed far out-of-equilibrium (by the incident light) distinct to that of the close-to-equilibrium vdPw measurements. Furthermore, photo-induced anomalous Hall currents only manifest when time-reversal symmetry is explicitly broken by the incident circularly polarized light. This contrasts with the time-reversal-symmetry of the non-irradiated GBG system used in vdPW measurements.
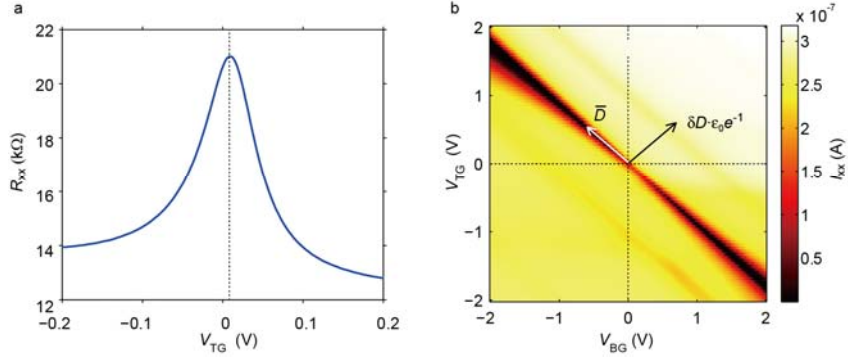
Fig. S1. Transport measurement (a) Top gate-dependent resistance when bottom gate voltage is 0 V. The offset of maximum resistance is around 0.01 V. This small value implies a high quality of our device. (b) Drain current with respect to top and bottom gate voltage. The source-drain bias is at 1 mV with frequency at 177 Hz. The arrows indicate the axis directions of $\bar{D}$ and $\delta D \cdot \varepsilon_0 e^{-1}$. We use $\delta D \cdot \varepsilon_0 e^{-1}$ (ε_0 and e are vacuum permittivity and elementary charge) as axis instead of δD, because it equals to free carrier density injected by gates when $\bar{D} = 0$. However, when $\bar{D} \neq 0$, $\delta D \cdot \varepsilon_0 e^{-1}$ is larger than the free carrier density, as some of the δD-injected charge carriers are immobile and drive Fermi level across the band gap. The thicknesses of top and bottom dielectric BN layers are 7.2 nm and 8.2 nm, respectively.
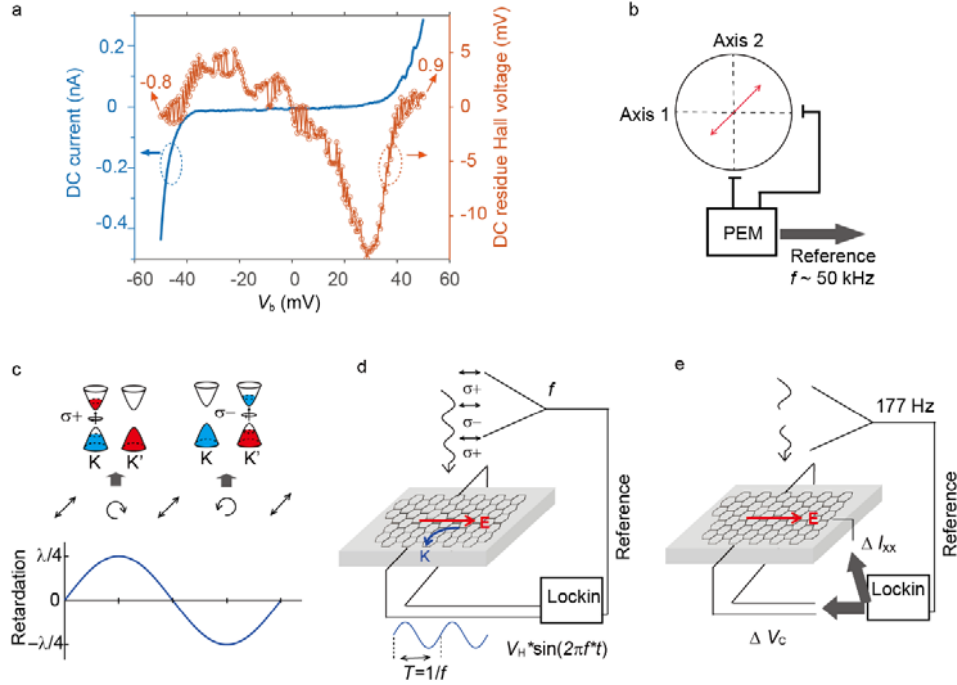
Fig. S2. Measurement mechanism. (a) Typical Remaining DC Hall voltage. Blue curve with left y axis is current-bias (I-V) curve of gapped bilayer graphene with band gap $E_g \sim 130$ meV. Orange circles with right y axis are remaining DC Hall voltages. The remaining Hall voltage suggests that DC measurements are not suitable for valley selective Hall measurements. (b) Polarization direction of incident laser with respect to optical axes of photoelastic modulator (PEM). The polarization direction is indicated by red arrow and has 45 degrees with respect to axes of PEM. The PEM changes the retardation between axis 1 and 2 with reference $f \approx 50$ kHz. (c) Chirality modulation by PEM. At retardation of $\lambda/4$ and $-\lambda/4$, the output beam shows right and left circular polarization, respectively. They selectively excite photocarriers at K or K' valleys. The change of chirality has frequency of $f \approx 50$ kHz. The light intensity is not changed during modulation (d). Illustration of our measurement setup. Photons with right circular polarization give rise to positive valley selective Hall voltage via K valley excitation, while photons with left circular polarization introduce negative valley selective Hall voltage. Modulating the chirality of circular polarization gives rise to valley selective Hall voltage at the same frequency of about 50 kHz. (e) The measurement of longitudinal photocurrent ΔI_{xx} or conventional photovoltage (ΔV_C) at Hall bar contacts. The intensity modulation is achieved by optical chopper at 177 Hz. Lockin amplifier was used to measure ΔI_{xx} or ΔV_C with reference signal from chopper.
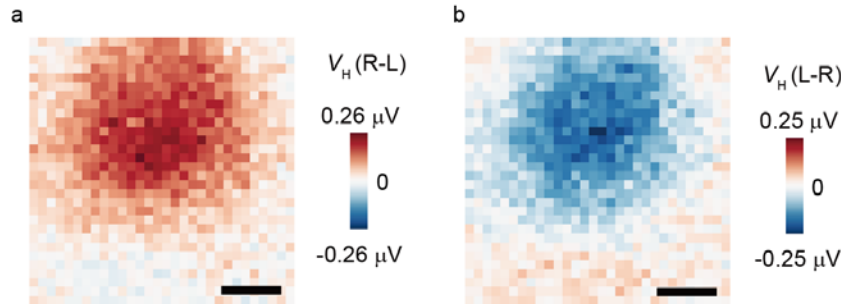
Fig. S3. Valley selective Hall voltages V_H for opposite modulation sequence. (a) Spatial map of V_H at modulating sequence of right to left (R-L) circular polarization. The modulating frequency is about 50 kHz. (b) The V_H map that is similar with panel a but at opposite chirality modulating sequence from left to right (L-R). The V_H shows opposite polarity to panel a, which agrees with equation 1 in main text. All the measurements were carried out at $E_g \approx 35$ meV with source-drain bias $V_b = 100$ mV.
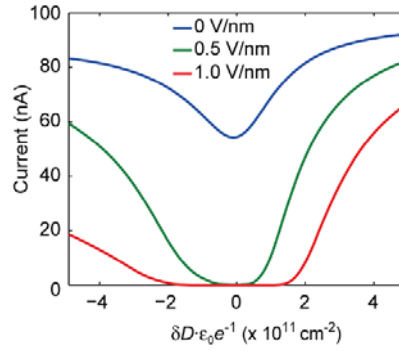
Fig. S4. Transfer curve of gapped bilayer graphene at different electrical displacement field $\overline{D}$. The source-drain bias V_b is 1 mV at 177 Hz. The signal is firstly pre-amplified and then measured by lockin amplifier. At $\overline{D} = 0.5$ V nm^{-1} and $\overline{D} = 1.0$ V nm^{-1}, plateaus of nearly zero drain current indicate gap-induced insulating states.
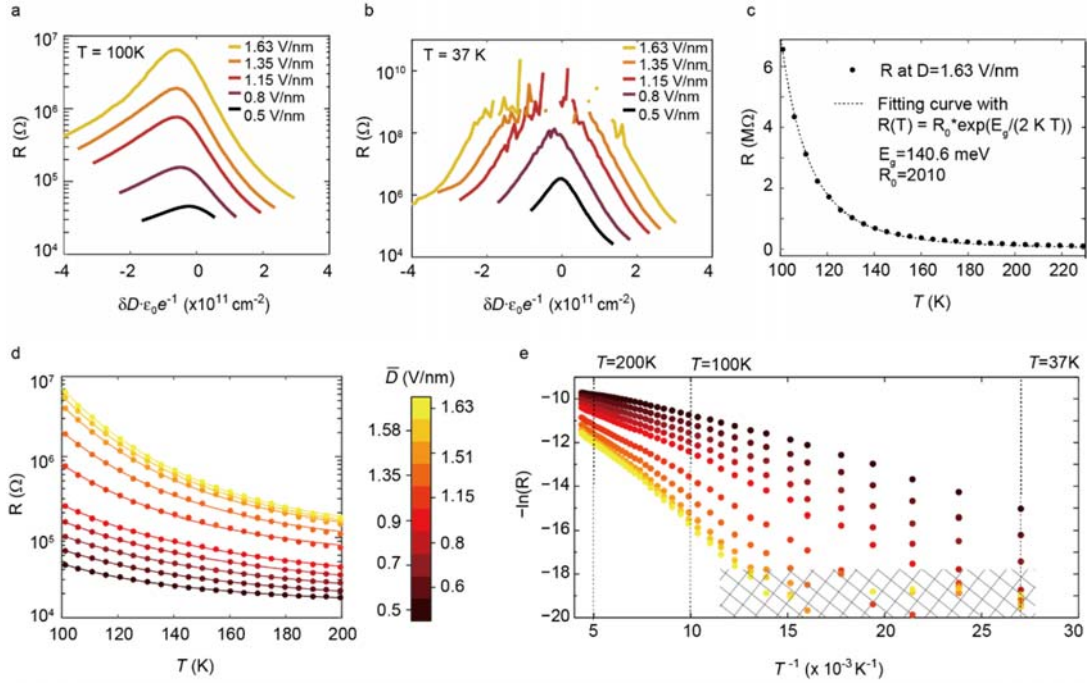
Fig. S5. Temperature-dependent resistance at various displacement fields. (a) Carrier density-dependent resistance at different electrical displacement field ($\bar{D}$). Temperature $T = 100$ K (b) The same measurements as panel a except at $T = 37$ K. Resistance goes beyond the range of our measurement system at higher displacement field. (c) Fitting curve with thermal activation (TA) model at $\bar{D} = 1.63$ V nm^{-1}. Resistances in the range of 100 - 200 K are used to extract a band gap of 140.6 meV. The resistance at each T is measured at the charge neutrality point, so the resistance here is maximum value at each T. (d) Resistance and TA fitting at different $\bar{D}$. Logarithmic y axis was used to fully show the agreement between data and fitting curves. (e) Arrhenius plot of resistance with y axis as natural logarithm of resistance and x axis as $1/T$. Meshed area labels abnormal data due to the limited range of our measurement system as also shown in panel b.
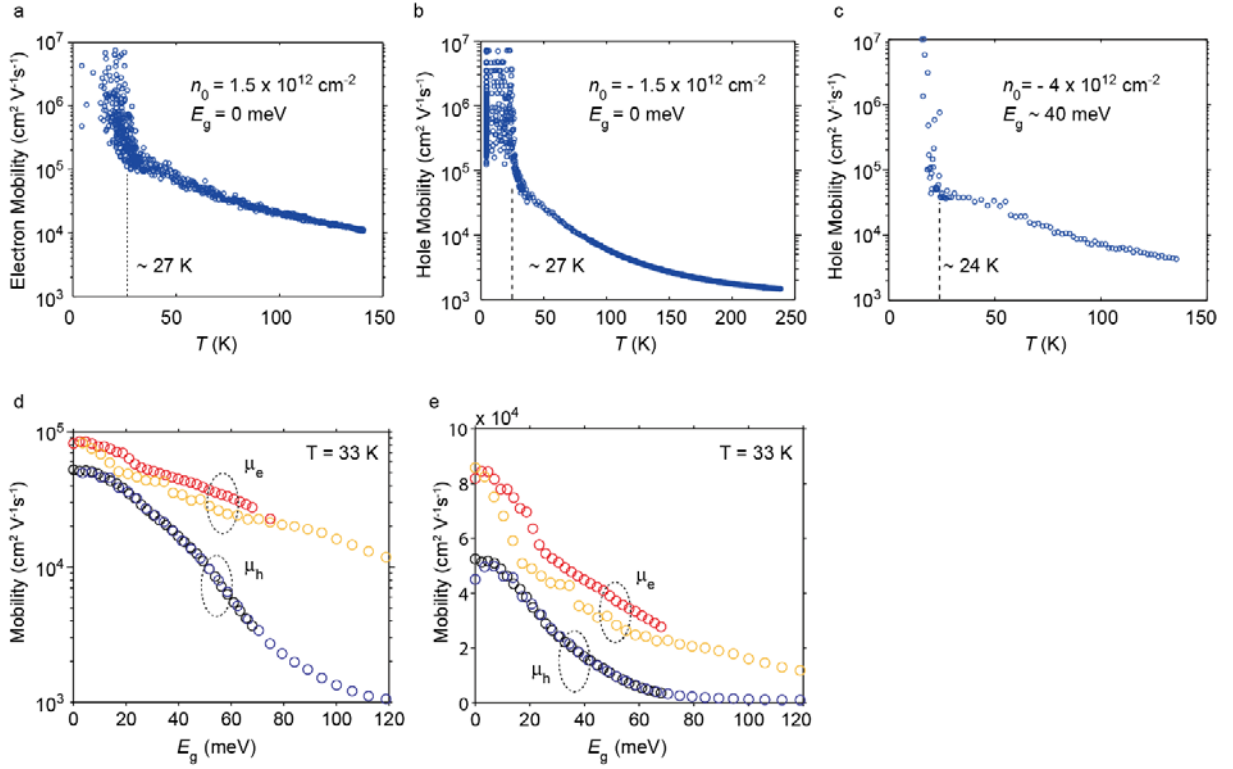
Fig. S6. Mobility (μ) of gapped bilayer graphene. Van der Pauw method is used to measure temperature (T)-dependent carrier mobility of bilayer graphene with (a) zero gap $E_g = 0$ meV and gate-induced electron density $n_0 = 1.5 \times 10^{12}$ cm^{-2} (b) $E_g = 0$ meV and $n_0 = -1.5 \times 10^{12}$ cm^{-2} (c) E_g ~ 40 meV and $n_0 = -4 \times 10^{12}$ cm^{-2}. At temperature lower than 24~27 K as indicated by dashed lines, the voltage drop across the device is very small yielding large apparent values of mobilities; these features may arise from a transition to a ballistic regime. We note, however, in our analysis, we consistently work with temperatures higher than that corresponding to this regime. (d) Electron μ_e and hole μ_h mobility measured by transport measurements at $T \sim 33$ K. Red and black circles are measured with source-drain bias V_b at 1 mV. Orange and blue circles are measured with V_b that ranges from 1 mV to 90 mV for different E_g. The change of V_b here is due to the measurement circuit, which has a resistor (1 MΩ) in serial in order to protect the device from burning. This is further explained in caption of Fig. S9a. (e) The same mobility data with panel e with logarithmic y axis.
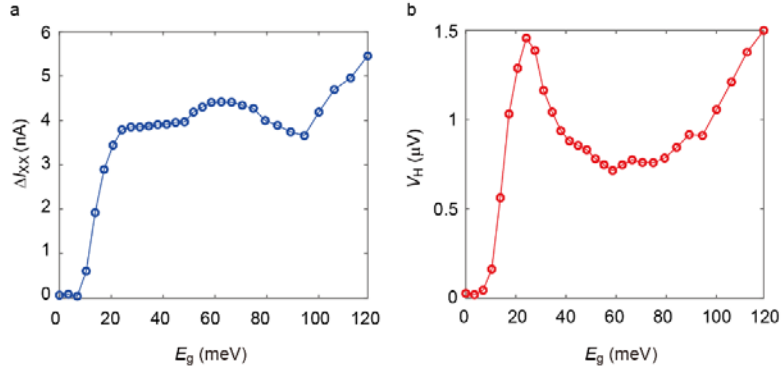
Fig. S7. Gap-dependent valley selective Hall voltage V_H and longitudinal photocurrent ΔI_{xx}
(a) and (b) Vertical linecuts of Fig. 2E (ΔI_{xx} map) and Fig. 2F (V_H map) around neutrality points
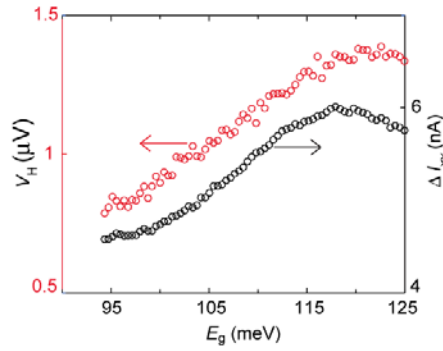at $\delta D \cdot \varepsilon_0 e^{-1} \approx 2.8 \times 10^{10}$ cm^{-2}.

Fig. S8. Valley selective Hall voltage V_H and longitudinal photocurrent ΔI_{xx} at resonant
absorption. They both show maximum values at resonance absorption. Parameters are $V_b = 50$ mV,
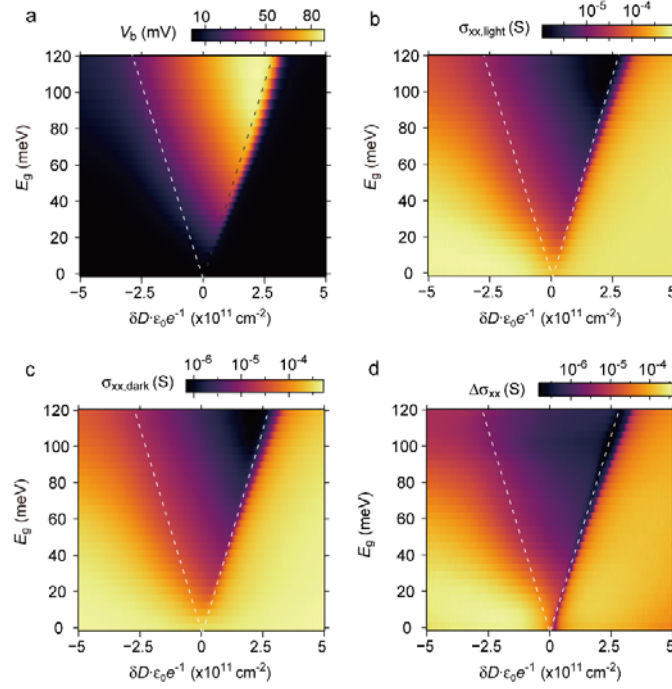$h\nu = 122.9$ meV, $P = 1.4$ µW µm^{-2}.

16

Fig. S9. Source-drain voltage V_b and Longitudinal conductivity σ_{xx}. (a) Distribution of V_b among states with different δD and E_g values, in which x axis is $\delta D \cdot \varepsilon_0 e^{-1}$ (ε_0 and e are vacuum permittivity and elementary charge). V_b changes with E_g and $\delta D \cdot \varepsilon_0 e^{-1}$ because a resistor (1 MΩ) is connected in series with the device, which protects the device from burning by relieving the voltage drop at the device when gapped bilayer graphene is doped (conductive). V_b shows higher value in the triangle area, where the Fermi level is inside the gap and the gapped bilayer graphene in insulating. The axes are explained in Method. (b) Longitudinal conductivity $\sigma_{xx,light}$ with laser ($h\nu = 122.9$ meV, $P = 1.4$ μW μm^{-2}) on. (c) Longitudinal conductivity $\sigma_{xx,dark}$ without illumination. (d) Longitudinal photoconductivity $\Delta\sigma_{xx} = \sigma_{xx,light} - \sigma_{xx,dark}$. The photoconductivity shows higher values outside the gap.
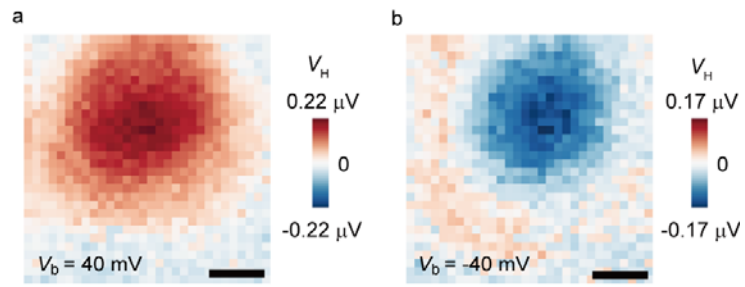
Fig. S10. Opposite valley selective Hall voltage (V_H) at opposite source-drain bias (V_b). (a) V_b= 40 mV. (b) V_b = - 40 mV. Based on equation 1, the polarity of source-drain bias is directly linked to the polarity of valley selective Hall voltage. The data is measured at E_g= 35 meV. The scale bars indicate 10 μm.
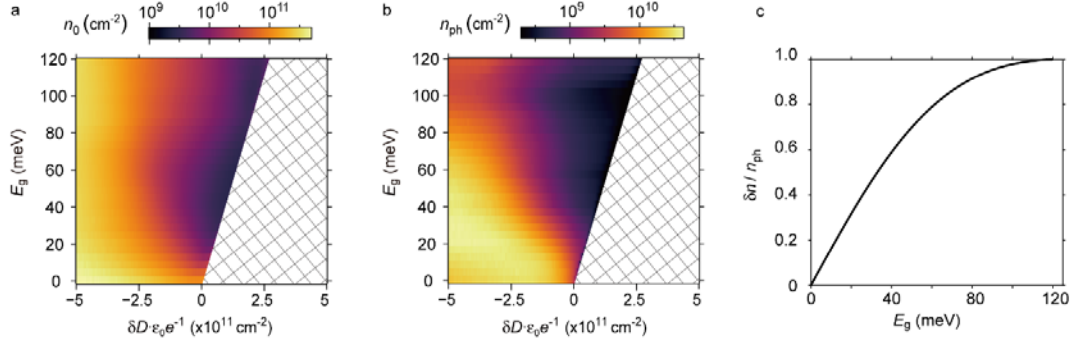
Fig. S11. Initial carrier density before excitation (n_0) and photocarrier density (n_{ph}). (a) Distribution of n_0 among states with different δD and E_g values. The x axis is $\delta D \cdot \varepsilon_0 e^{-1}$. At $V_b = 0$ and $\overline{D} = 0$ ($E_g = 0$), $\delta D \cdot \varepsilon_0 e^{-1}$ precisely equals to gate-injected carrier n_0, whereas at $\overline{D} \neq 0$ ($E_g \neq 0$), $\delta D \cdot \varepsilon_0 e^{-1}$ becomes smaller than n_0, because part of $\delta D \cdot \varepsilon_0 e^{-1}$ is consumed for moving Fermi level out of band gap. With the presence of source drain bias ($V_b \neq 0$), especially V_b is comparable with E_g, it introduces additional charge carriers and elevate conductivity. The whole n_0, including gate and bias induced charge carriers, is calibrated by using $\sigma_{xx} = n_0 e \mu$, in which μ is hole mobility as calculated in Fig. S6. Here, only n_0 values at hole side (trapezoid) is calibrated and then used for calculating valley selective Hall conductivity σ_H in Fig. 4 in main text. (b) Distribution of n_{ph} among states with different δD and E_g values. For each E_g, n_{ph} is calculated by dividing $\Delta\sigma_{xx}$ in Fig. S9d with average mobility $\mu_{ave} = (\mu_e + \mu_h)/2$ (μ_e and μ_h are orange and blue circles in Fig. S6d), as photocarriers include both electrons and holes. (c) The gap-dependent photocarrier imbalance (δn) between K and K' valleys that is used in the theoretical models in Fig. 4. The imbalance is caused by photoexcitation from circularly-polarized laser due to the valley selection rule, and defined as $\delta n = \left| n_{ph}^K - n_{ph}^{K'} \right|$, in which n_{ph}^K ($n_{ph}^{K'}$) is photocarrier densities at K (K') valley and $n_{ph} = n_{ph}^K + n_{ph}^{K'}$. This dependence is based on the simple estimate as shown in equation S15.
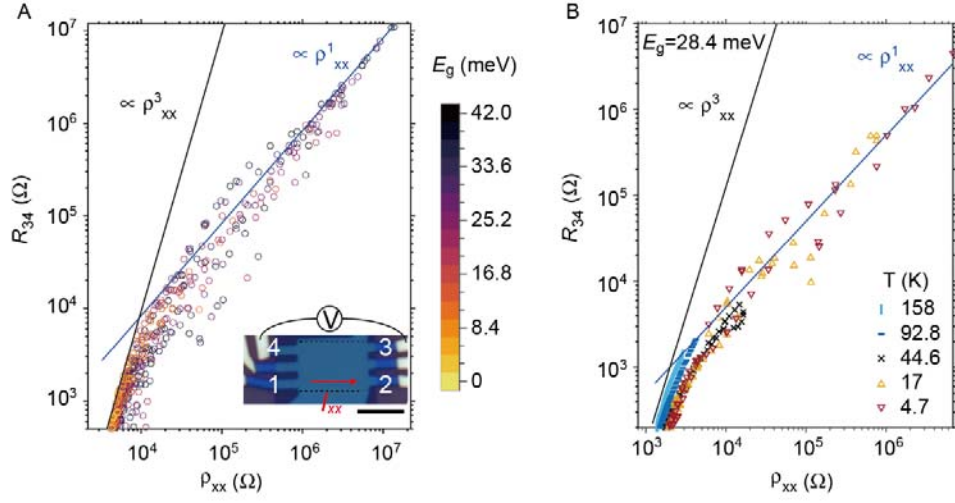
Fig. S12. Van der pauw (vdPw) measurement of device 2 (A) vdPw resistance R_{34} vs. longitudinal resistivity ρ_{xx} at different band gaps E_g. The vdPw resistance is defined as $R_{34} = V_{34}/I_{xx}$, in which V_{34} is voltage between terminal 3 and 4, and I_{xx} is current injected from terminal 1 to 2, as shown in an inset figure. ρ_{xx} is calculated as $\rho_{xx} = \alpha * V_{12}/I_{xx}$, where α is estimated as 0.157 based on a diffusive model (*39*). Blue and black lines indicate scaling relations of $R_{34} \propto \rho^1_{xx}$ and $R_{34} \propto \rho^3_{xx}$. The scale bar of inset figure indicates 5 μm. The dashed lines in inset figure indicate bilayer graphene channel region. (B) R_{34} vs. ρ_{xx} at different temperatures while E_g is fixed at 28.4 meV. Blue and black lines indicate scaling relations of $R_{34} \propto \rho^1_{xx}$ and $R_{34} \propto \rho^3_{xx}$.